Broadband pyramid antireflective structure on chalcogenide glasses by the hot embossing method for infrared photonics

LIZHU LI,[1,2,*] ⊙ JULIEN ARI,[1,3] PIERRE A. DEYMIER,[1] AND PIERRE LUCAS[1]

[1]*Department of Materials Science and Engineering, University of Arizona, Tucson, AZ 85721, USA*
[2]*Currently with James C. Wyant College of Optical Sciences, University of Arizona, Tucson, AZ 85721, USA*
[3]*Currently with Institut de Chimie Moléculaire et des Matériaux d'Orsay (ICMMO), Université Paris-Saclay, CNRS, 91405 Orsay, France*
[*]*lizhuli@email.arizona.edu*

Abstract: Pyramidal antireflective structures were produced by hot embossing single- and double-sides of an amorphous $GeSe_4$ optical element. The optical performances were measured across the wavelength range from 2 μm to 15 μm. The transmittance at normal incident angle was increased up to 75.6% and 79.8% for single and double-side embossing respectively. The experimental results were in close agreement with simulation performed using the rigorous coupled-wave analysis (RCWA). Theoretical models also predicted well the transmittance changes as a function of incident angle from 0 ° to 50 ° at a fixed laser wavelength of 5.1 μm. A Fabry-Perot interferometer consisting of two single surface embossed samples is proposed.

1. Introduction

Chalcogenide glasses have been ideal candidates for many optical applications due to their broad transparency window, low phonon energy, high nonlinearity, and high refractive indices [1]. The high refractive indices are due to the large atomic polarizability of chalcogen elements (sulfur, selenium and tellurium) [2]. The high refractive indices of these chalcogenide glasses are advantageous for strong optical confinement. It enables small waveguide dimensions and enhances optical intensities for nonlinear interactions [3–6]. However, the main disadvantage of high refractive indices is the large Fresnel reflection at the interface between air and chalcogenide material [7]. Approximately, 17% of the light will be reflected at the interface when light travels between air and $GeSe_4$ glass [8]. The excessive reflected light is disadvantageous for many applications in several aspects [9–11]. Firstly, it reduces the throughput of an optical system and limits its operational efficiency. Secondly, it may induce ghost images and reduce the quality of resulting images in an optical imaging system. Thirdly, it will reduce the stability of an optical system.

One method to reduce the reflection is to apply multilayer antireflective coatings [12,13]. $Ge_{1-x}C_x$ film combined with diamond-like carbon film deposited on As_2Se_3 glass by radio frequency sputtering technique have been demonstrated to improve the average transmittance of As_2Se_3 glass from 62.2% to 72.6% within the wavelength range from 3 μm to 5 μm [14]. Multilayer of ZnS films with high refractive index and YbF_3 films with low refractive index deposited on $Ge_{28}Sb_{12}Se_{60}$ glass by electron beam evaporation technique have been demonstrated to increase the transmittance of $Ge_{28}Sb_{12}Se_{60}$ glass up to 97.4% within the wavelength range from 3.5 μm to 4.5 μm [15]. However, the multilayer antireflective coating method suffers from several disadvantages [16–19]. Firstly, it requires expensive and complicated instrumentation to deposit exotic materials. This leads to low production efficiency and high cost. Secondly, the maximum number of layers that can be applied is limited by deposition techniques and

properties of thin film materials and chalcogenide substrate. Thirdly, the poor adhesion between the chalcogenide substrate and multilayer coatings can lead to delamination.

Another emerging method to reduce the reflection is to apply micro/nano antireflective structures by hot embossing method [20–24]. This technology has several advantages, such as low cost, simple process and high efficiency. The embossed antireflective structures have the same composition and properties as the bulk material. As a result, the disadvantages suffered by the antireflective coating technology are eliminated. Besides, antireflective structures provide higher laser-induced damage threshold than that of traditional antireflective-coated surfaces [17]. It is important for high power laser light delivery using chalcogenide fibers. One of the most widely used antireflective structure is moth-eye structure [20–24]. It has been hot embossed on As_2Se_3 glass from a customized master mold to improve the transmittance of As_2Se_3 glass from 64% to 76% [22]. It has also been hot embossed on $As_{39.4}Se_{60.6}$/$As_{38.6}Se_{61.4}$ core/clad fiber from a customized master mold to improve the transmittance of the fiber up to 70.74% after single side embossing and 88.3% after two sides embossing [24]. Another extensively used antireflective structure is pyramidal structure [25]. The theoretical performance of pyramidal antireflective structure on As_2S_3 glass was simulated within the wavelength range from 2 μm to 5 μm [21]. However, to the best of the authors' knowledge, pyramid antireflective structure hot embossed on chalcogenide glass has not been experimentally demonstrated yet.

In this paper, selection criteria are considered for optimal hot embossing of chalcogenide glasses. The fabrication of hot embossed pyramid-shaped antireflective structures on environmentally friendly $GeSe_4$ glass is then demonstrated. Its optical performance is investigated in the important molecular fingerprint wavelength region from 2 μm to 15 μm. The transmittance is characterized as a function of wavelength at normal incident angle and as a function of incident angle ranging from 0 ° to 50 ° at a fixed laser wavelength of 5.1 μm. The experimental results are compared with simulation results obtained by rigorous coupled-wave analysis (RCWA) method. A Fabry-Perot interferometer consisting of two single surface embossed sample is proposed and the simulated performances are investigated.

2.　Fabrication

Materials selection for the fabrication of embossed devices follows several criteria. The first criterion is related to the non-toxicity and environmentally benign nature of the material. A chalcogenide glass from the Ge-Se system containing no arsenic or antimony is therefore selected. The second criterion relates to the glass stability against crystallization of the selected composition. This is crucial to avoid any nucleation during the embossing process which could lead to scattering. Ge-rich compositions are prone to crystallization during reheating [8] and should therefore be avoided. But Se-rich compositions tend to have low glass transition temperatures T_g which could be unpractical. Hence, an intermediate composition is preferred. The third criterion is more specific to the fabrication method and involves the concept of fragility (Fig. 1(a)). Upon heating above T_g, fragile glass-formers exhibit a rapid drop in viscosity while strong glass-formers show a shallower near-Arrhenius dependence of viscosity with temperature. As depicted in Fig. 1(a), small changes in temperature lead to large variation in viscosity for fragile systems. This is a detrimental feature that leads to unstable processing conditions. Hence, a glass composition exhibiting a strong viscosity behavior is favored. Recent reviews of the Ge_xSe_{1-x} system [26] indicate that the composition with lowest fragility index m occurs for x= 20-25%, as shown in Fig. 1(b). Considering all these criteria a glass of composition $GeSe_4$ was selected for this study.

Figure 2(a) depicts the hot embossing setup. During the hot embossing process, the mold and flat polished chalcogenide glass are heated up to 230 °C. This temperature is 65 °C higher than the glass transition temperature of $GeSe_4$ of 165 °C measured by differential scanning calorimetry. At this temperature the viscosity of $GeSe_4$ is $\eta \sim 10^8$ Pa·s [27]. It is noted that this value is significantly higher than conventional fiber drawing viscosity for chalcogenide glasses
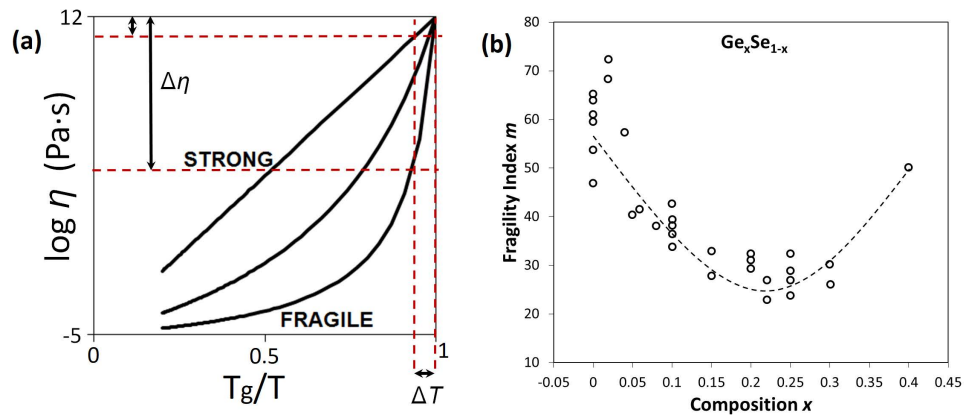
Fig. 1. (a) Schematics of a fragility plot showing the viscosity-temperature dependence of strong versus fragile glass formers and the relative change in viscosity for a temperature increase ΔT. (b) Fragility index m as a function of Ge% in the Ge-Se system (adapted from Ref. [26]).

i.e. $\eta \sim 10^5$ Pa·s for As_2Se_3 [28]. The present range of viscosity enables the pattern transfer from the master mold to a circular disk sample with a diameter of 6.03 mm and a thickness of 2.41 mm by gradually increasing the applied force up to 60 kg. The applied pressure is 20.59 N/mm^2 and maintained for 20 minutes. The sample is then cooled down and once the temperature reaches below 165 °C, the force is gradually reduced, and a single side embossed glass window is released. A double side embossed sample is achieved by applying the above procedures on both sides of a flat polished sample.
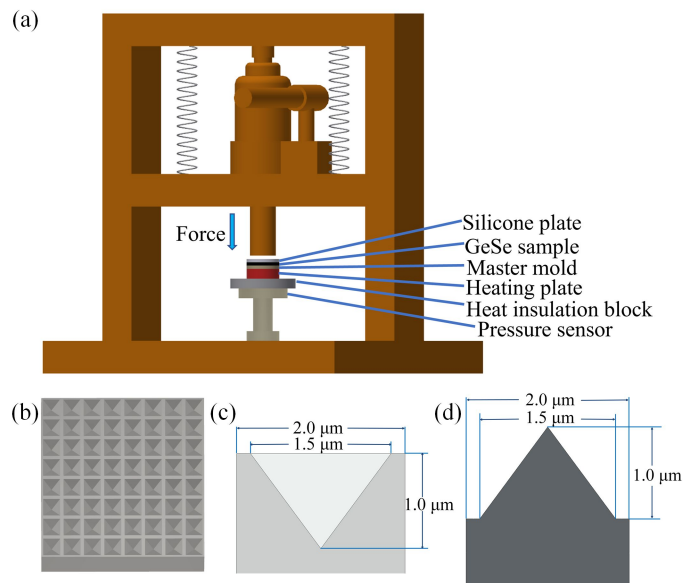

Fig. 2. (a) Embossing setup; (b) Schematics of Klarite 302 master mold; (c) Dimensions of a single inverted pyramid; (d) Dimensions of an embossed pyramid.

In order to confirm that no structural or compositional changes occurred during the process, Raman spectroscopy was performed on the glass sample surface before and after embossing. Figure 3 indicates that the Raman spectra are identical within the limits of experimental error. This implies that the stoichiometry and phase of the $GeSe_4$ glass do not change during embossing.
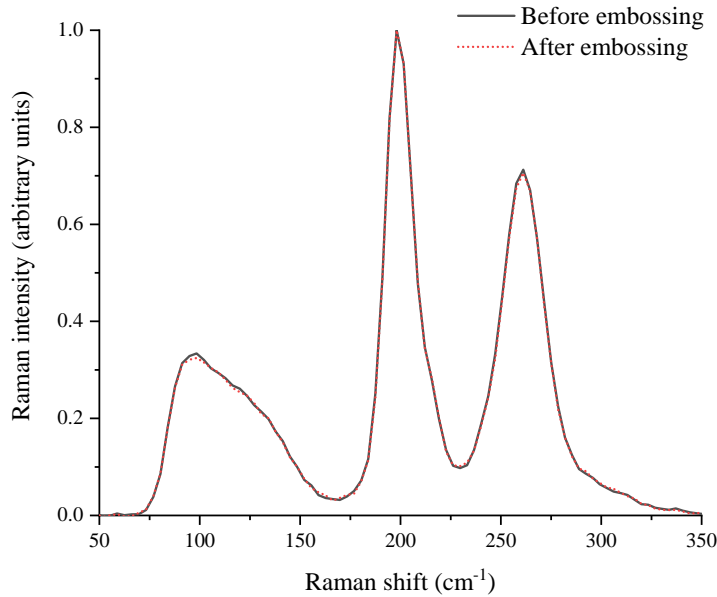
Fig. 3. Raman spectra of $GeSe_4$ sample surface before and after embossing.

Antireflective structures with a pyramidal shape are highly desirable to reduce the high Fresnel reflection at the air-$GeSe_4$ interface. The period p should be less than the minimum wavelength inside the wavelength range of interest over the refractive index of $GeSe_4$ glass based on the 0th order grating condition. It implies the period p should be less than 2.08 μm to guarantee 0th order transmittance when the wavelength of incident light is larger than 5 μm [29]. Considering the constraints of manufacture, the chosen period should be slightly less than 2.08 μm. Normally, fabrication of a customized master mold is required for hot embossing process [22–24]. In the present case, Klarite 302, a commercially available surface enhanced Raman scattering substrate, satisfies the requirement for 0th order grating condition and ease of fabrication. The Klarite 302 is fabricated using the well-developed lithographic process in semiconductor manufacturing. The inverted pyramidal pattern was etched into a silicon substrate and then coated with a layer of gold. The Klarite 302 substrate shown in Fig. 2(b) consists of arrays of inverted pyramids with a period of 2 μm, a square base of length of 1.5 μm and a depth of 1.0 μm (Fig. 2(c)). The spacing between two consecutive inverted pyramids is therefore 0.5 μm. A scanning electron microscope (SEM) image of the Klarite 302 mold is shown in Fig. 4(a). The resulting antireflection pattern embossed on the $GeSe_4$ glass surface is shown in Fig. 4(b) and (c). The pyramidal pattern is imprinted on the glass surface with high consistency. Exposure of the imprinted area to visible light results in diffraction due to the periodic arrays of pyramids as shown in Fig. 4(d).
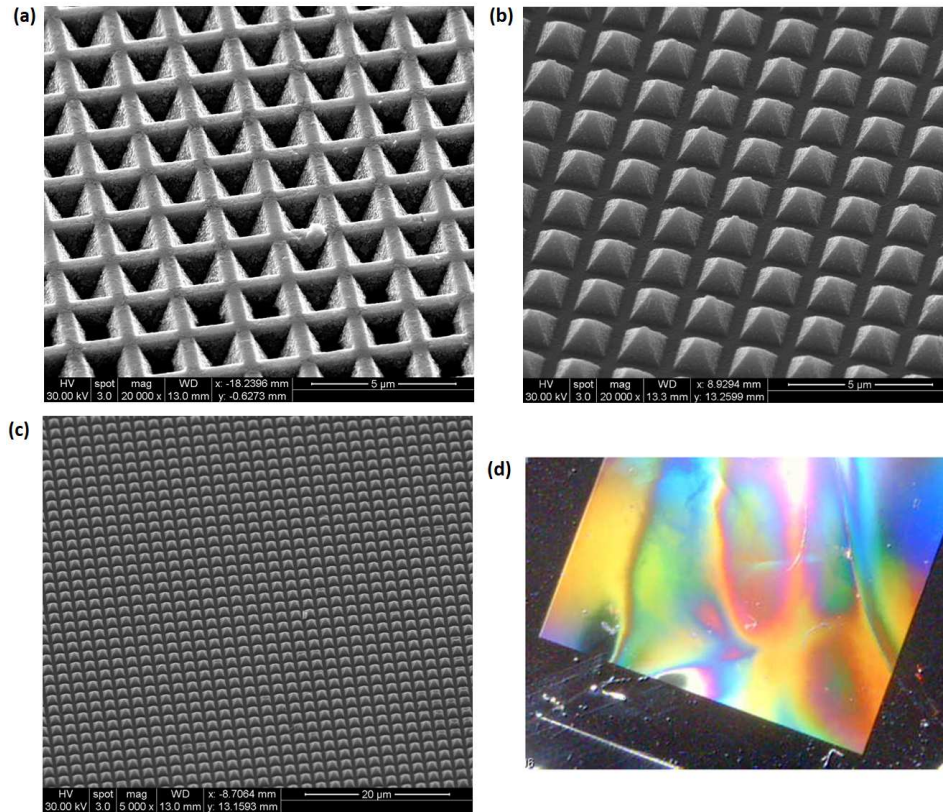
Fig. 4. (a) SEM image of the Klarite 302 mold; (b,c) SEM images of the pyramidal antireflective structures embossed on the surface of a GeSe$_4$ disc. (d) Visible image of the embossed area showing light diffraction due to pyramid arrays. The embossed area is 4 mm x 4 mm.

3. Characterization and modeling

Fourier-transform infrared spectroscopy was used to measure the transmittance of all samples at normal angle across the wavelength range from 2 μm to 15 μm. Figure 5 compares the measured transmittance of the flat polished sample, single-side embossed sample and double-side embossed sample. As expected, the single-side and double-side embossed samples show an increased transmittance with a maximum at 5.03 μm. The transmittance of the flat polished sample, input-side embossed sample and both-surface embossed sample was 68.6%, 75.6% and 79.8%, respectively, at a wavelength of 5.03 μm. The absorption dip around 13 μm is due to an overtone of the fundamental network vibration and is an intrinsic feature of the GeSe$_4$ glassy backbone [30].

In order to rationalize these experimental results, a theoretical model was used to simulate the pyramid antireflective structures. The optical properties of the embossed structure were modeled using the geometric parameters for the pyramids shown in Fig. 2(d), i.e. height of 1 μm, base length of 1.5 μm, and period of pyramids structure of 2 μm. The refractive index of the GeSe$_4$ was set to 2.4, which was a good approximation to the experimentally measured value over the wavelength of interest [31]. As shown in Fig. 4 (b) and (c), the pyramids are squarely packed. A single unit simulation is therefore enough to predict the results of the whole structure based on the Floquet-Bloch theorem. The transmission of a unit cell was simulated
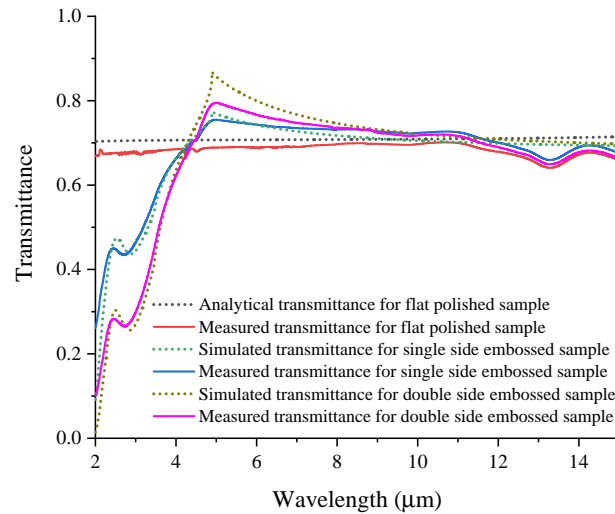
Fig. 5. Experimental and analytical/simulated 0th order transmittance of the flat polished sample, single side embossed sample and double side embossed sample.

with the commercial software package DiffractMOD, which uses the rigorous coupled-wave analysis (RCWA). Figure 5 shows the analytical transmittance of the flat polished sample, and simulated transmittance of single-side embossed sample and double-side embossed sample. The experimental results agree well with the simulated results for the single side embossed sample. The 0th order transmittance dramatically decreases for wavelengths smaller than 5 μm. This is because the 0th order grating condition is not satisfied when the wavelength of incident light is smaller than 5 μm. The embossed structure acts like a diffractive grating and leads to the dramatic decrease of the transmission. The pattern is well reproduced by the model. The slight mismatch between experimental results and simulation results within the wavelength range from 11.5 μm to 15.0 μm is due to the constant absorption coefficient used in the simulation.

The transmission of the double-side embossed sample should be higher near the maximum at 5.03 μm and it should be higher than that of the single-side embossed sample within the wavelength range from 9 μm to 16 μm. Disagreements between experiment and modeling of the double-side embossed sample are likely due to the misalignment, such as offset and/or misorientation, between the pyramids structure on both surfaces of the experimental sample. Nevertheless, the transmission near 5.03 μm is still higher for double-side than single-side embossed sample, as expected.

Figure 6 shows the measured 0th order transmittance of the flat polished $GeSe_4$ sample and single side embossed $GeSe_4$ sample as a function of incident angle. It was measured with a mid-infrared laser with a central wavelength of 5.1 μm and p polarization state and a HgCdTe detector. The experimental results agreed well with the simulation results. The maximum transmittance increase of the input-side embossed sample was 6.5% when the incident angle was at normal. The transmittance of p polarization light of the flat polished and single side embossed $GeSe_4$ sample gradually increased with the increase of the incident angle since it moved toward the Brewster angle.
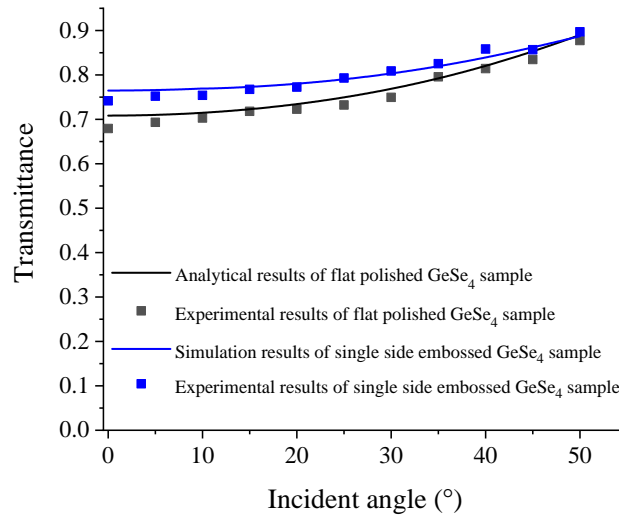
Fig. 6. The measured 0th order transmittance within the incident angle range from 0 ° to 50 ° when the laser had a central wavelength of 5.1 µm and p polarization state.

4. Device modeling

The ability to easily manufacture embossed antireflective structure could be of great benefit for the design of Fabry-Perot (FP) etalon. The proposed FP etalon consists of two facing elements with parallel surfaces and input and output surfaces embossed with pyramid shape antireflective structures. Figure 7 shows the typical FP cavity with flat surfaces, typical FP cavity with tilted surfaces and proposed FP cavity with embossed surfaces. The typical FP cavity with flat surfaces suffers from multireflection and ghost image. To avoid unwanted etalon effects caused by the reflections from the outside surfaces of the components, the air spaced etalons require the outside surfaces of the component to be wedged and coated with multilayer anti-reflective coating, as shown in Fig. 7(b). These involve polishing process to fabricate wedged shape and thin film deposition processes, which are time consuming and expensive. Instead, the proposed structure, shown in Fig. 7(c), does not suffer from complicated polishing procedures and expensive film deposition processes. The input and output surfaces can readily be hot embossed with pyramid shape antireflective structures.

Fig. 7. (a) typical FP cavity with flat surfaces (b) typical FP cavity with tilted surfaces (c) FP cavity with embossed surfaces.

The two parallel surfaces of the two embossed samples form an air-space FP etalon. The etalon uses the 17% Fresnel reflection at each interface to provide the etalon effect. Figure 8 shows the simulated transmittance of GeSe$_4$ FP etalon with embossed input and output surfaces. Such an etalon could be used inside a mid-infrared laser cavity to filter out unwanted laser wavelengths.

The benefit of this structure includes minimizing fabrication complexity and maximizing the FP etalon robustness.
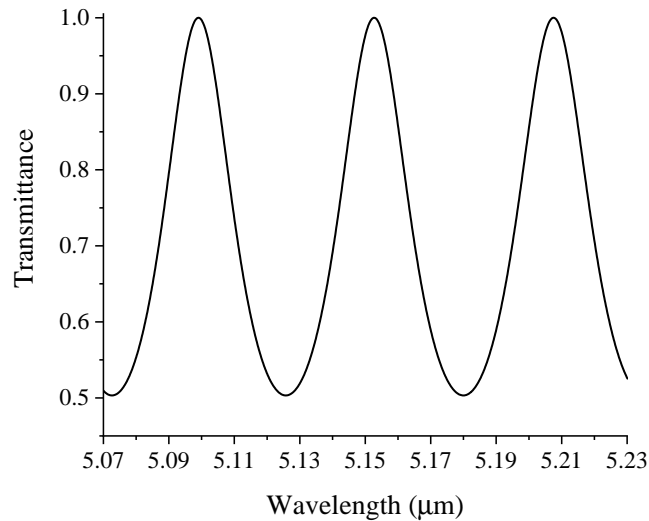
Fig. 8. Simulated transmittance of a GeSe$_4$ FP etalon with embossed input and output surfaces.

5.   Conclusion

We have demonstrated the fabrication of pyramid shape antireflective structure, replicated from a commercially available master mold, on GeSe$_4$ glass via hot embossing method. The measured transmittance of the single side and double side embossed sample increased by up to 7% and 11.2%, respectively, within the wavelength range from 5 μm to 15 μm at normal incidence. The measured transmittance of p polarization light at 5.1 μm of the single-side embossed sample increased by up to 6.5% for incident angles ranging from 0 ° to 50 °. The experimental results agreed well with the simulation results using RCWA method. One critical advantage of the antireflective structures is that the effective refractive index at the interface area could be precisely tuned to a value between the air and the bulk GeSe$_4$ sample by modifying the period, height and profile of the structures. Another critical advantage of the antireflective structure is its broadband antireflective property and wide range of incidence angles. The pyramid shaped antireflective structures could be applied to many chalcogenide glasses with refractive index larger than that of GeSe$_4$ glass by hot embossing method. It can reduce the high Fresnel reflection and increase the output efficiency of optical systems.

References

1. B. Bureau, X. Zhang, F. Smektala, J. Adam, J. Troles, H. Ma, C. Boussard-Plèdel, J. Lucas, P. Lucas, D. L. Coq, M. R. Riley, and J. Simmons, "Recent advances in chalcogenide glasses," J. Non-Cryst. Solids **345-346**, 276–283 (2004).
2. A. B. Seddon, "Chalcogenide glasses: a review of their preparation, properties and applications," J. Non-Cryst. Solids **184**, 44–50 (1995).
3. P. Lucas, M. A. Solis, D. L. Coq, C. Juncker, M. R. Riley, J. Collier, D. E. Boesewetter, C. Boussard-Plédel, and B. Bureau, "Infrared biosensors using hydrophobic chalcogenide fibers sensitized with live cells," Sens. Actuators, B **119**(2), 355–362 (2006).
4. L. Li, A. Al-Kadry, N. Abdukerim, and M. Rochette, "Design, fabrication and characterization of PC, COP and PMMA-cladded As_2Se_3 microwires," Opt. Mater. Express **6**(3), 912–921 (2016).
5. A. Al-Kadry, L. Li, M. EI Amraoui, T. North, Y. Messaddeq, and M. Rochette, "Broadband supercontinuum generation in all-normal dispersion chalcogenide microwires," Opt. Lett. **40**(20), 4687–4690 (2015).
6. D. D. Hudson, S. Antipov, L. Li, I. Alamgir, T. Hu, M. EI Amraoui, Y. Messaddeq, M. Rochette, S. D. Jackson, and A. Fuerbach, "Toward all-fiber supercontinuum spanning the mid-infrared," Optica **4**(10), 1163–1166 (2017).
7. Y. Fang, D. Jayasuriya, D. Furniss, Z. Q. Tang, L. Sojka, C. Markos, S. Sujecki, A. B. Seddon, and T. M. Benson, "Determining the refractive index dispersion and thickness of hot-pressed chalcogenide thin films from an improved Swanepoel method," Opt. Quantum Electron. **49**(7), 237 (2017).
8. G. Yang, Y. Gueguen, J. C. Sangleboeuf, T. Rouxel, C. Boussard-Plédel, J. Troles, P. Lucas, and B. Bureau, "Physical properties of the Ge_xSe_{1-x} glasses in the $0<x<0.42$ range in correlation with their structure," J. Non-Cryst. Solids **377**, 54–59 (2013).
9. R. E. Wagner and C. R. Sandahl, "Interference effects in optical fiber connections," Appl. Opt. **21**(8), 1381–1385 (1982).
10. A. L. Kano, A. R. Rouse, and A. F. Gmitro, "Ultrathin single-channel fiberscopes for biomedical imaging," J. Biomed. Opt. **18**(1), 016013 (2013).
11. Y. Matsuoka, M. P. Semtsiv, S. Peters, and W. T. Masselink, "Broadband multilayer antireflection coating for quantum cascade laser facets," Opt. Lett. **43**(19), 4723–4726 (2018).
12. H. K. Raut, V. A. Ganesh, A. S. Nair, and S. Ramakrishna, "Anti-reflective coatings: a critical, in-depth review," Energy Environ. Sci. **4**(10), 3779–3804 (2011).
13. J. A. Dobrowolski and B. T. Sullivan, "Universal antireflection coatings for substrates for the visible spectral region," Appl. Opt. **35**(25), 4993–4997 (1996).
14. K. Fu, Y. Jin, C. Zu, K. He, B. Xu, H. Zhao, Y. Liu, and W. Chen, "The structure and properties of low temperature deposited durable infrared $Ge_{1-x}C_x$ films on $As_{40}Se_{60}$ chalcogenide glass," J. Non-Cryst. Solids **519**, 119453 (2019).
15. X. Fu, H. Jiang, J. Zhang, S. Xiong, K. Guo, and B. Sun, "Preparation of short and medium wave infrared anti-reflective coating based on chalcogenide glass," Chin. J. Lasers **44**(9), 0903002 (2017).
16. F. Lemarquis, T. Begou, A. Moreau, and J. Lumeau, "Broadband antireflection coatings for visible and infrared ranges," CEAS Space J. **11**(4), 567–578 (2019).
17. D. S. Hobbs, B. D. MacLeod, and J. R. Riccobono, "Update on the development of high performance anti-reflecting surface relief micro-structures," Proc. SPIE **6545**, 65450Y (2007).
18. K. M. Khajurivala, "Erosion resistant anti-reflection coating for ZnSe, CZnS, chalcogenide and glass substrates," Proc. SPIE **8012**, 801242 (2011).
19. J. H. Lee, H. Kim, W. H. Lee, M. C. Kwon, and Y. G. Choi, "Surface modification of chalcogenide glass for diamond-like-carbon coating," Appl. Surf. Sci. **478**, 802–805 (2019).
20. J. Sanghera, C. Florea, L. Busse, B. Shaw, F. Miklos, and I. Aggarwal, "Reduced Fresnel losses in chalcogenide fibers by using anti-reflective surface structures on fiber end faces," Opt. Express **18**(25), 26760–26768 (2010).
21. R. J. Weiblen, C. R. Menyuk, L. E. Busse, L. B. Shaw, J. S. Sanghera, and I. D. Aggarwal, "Optimized moth-eye anti-reflective structures for As_2S_3 chalcogenide optical fibers," Opt. Express **24**(10), 10172–10187 (2016).
22. M. R. Lotz, C. R. Petersen, C. Markos, O. Bang, M. H. Jakobsen, and R. Taboryski, "Direct nanoimprinting of moth-eye structures in chalcogenide glass for broadband antireflection in the mid-infrared," Optica **5**(5), 557–563 (2018).
23. M. Lotz, J. Needham, M. H. Jakobsen, and R. Taboryski, "Nanoimprinting reflow modified moth-eye structures in chalcogenide glass for enhanced broadband antireflection in the mid-infrared," Opt. Lett. **44**(17), 4383–4386 (2019).
24. C. R. Peterson, M. B. Lotz, C. Markos, G. Woyessa, D. Furniss, A. B. Seddon, R. J. Taboryski, and O. Bang, "Thermo-mechanical dynamics of nanoimprinting anti-reflective structures onto small-core mid-IR chalcogenide fibers," Chin. Opt. Lett. **19**(3), 030603 (2021).
25. J. Cai and L. Qi, "Recent advances in antireflective surfaces based on nanostructure arrays," Mater. Horiz. **2**(1), 37–53 (2015).
26. A. Zeidler, P.S. Salmon, D. A. J. Whittaker, K. J. Pizzey, and A. C. Hannon, "Topological ordering and viscosity in the glass-forming Ge–Se system: the search for a structural or dynamical signature of the intermediate phase," Front. Mater. **4**, 32 (2017).
27. S. V. Nemilov, "Viscosity of oxygen-free vitrified systems. IV. Viscosity and structure of glasses in the selenium-germanium system," Zh. Prikl. Khim. (S.-Peterburg, Russ. Fed.) **37**, 1020–1024 (1964).
28. G. Yang, T. Rouxel, J. Troles, B. Bureau, C. Boussard-Plédel, P. Houizot, and J. C. Sangleboeuf, "Viscosity of As_2Se_3 glass during the fiber drawing process," J. Am. Ceram. Soc. **94**(8), 2408–2411 (2011).

29. W. H. Southwell, "Pyramid-array surface-relief structures producing antireflection index matching on optical surfaces," J. Opt. Soc. Am. A **8**(3), 549–553 (1991).

30. P. Lucas, S. Cui, D. P. Bayko, O. Gulbiten, G. J. Coleman, and J. Troles, "Homogeneity of melt-rocked Ge–Se glasses and the effect of impurities," Int. J. Appl. Glass Sci. **12**(3), 391–397 (2021).

31. L. G. Aio, A. M. Efimov, and V. F. Kokorina, "Refractive index of chalcogenide glasses over a wide range of compositions," J. Non-Cryst. Solids **27**(3), 299–307 (1978).